Self-Confined Nucleation of Iron Oxide Nanoparticles in a Nanostructured Amorphous Precursor

Jens Baumgartner, Raj-Kumar Ramamoorthy, Alexy Freitas, Marie-Alexandra Neouze, Mathieu Bennet, Damien Faivre, David Carriere

Self-confined nucleation of iron oxide nanoparticles in a nanostructured amorphous precursor

*Jens Baumgartner,[1,‡] Raj Kumar Ramamoorthy[2†], Alexy P. Freitas[2,3], Marie-Alexandra Neouze[3], Mathieu Bennet[1], Damien Faivre[1,4 *], David Carriere[2,‡*]*

[1]Department of Biomaterials, Max Planck Institute of Colloids and Interfaces, Science Park Golm, 14424 Potsdam, Germany.

[2]LIONS, NIMBE, CEA, CNRS, Université Paris-Saclay, CEA Saclay 91191 Gif sur Yvette Cedex France.

[3]Laboratoire de Physique de la Matière Condensée, École polytechnique, CNRS, Université Paris-Saclay, 91128, Palaiseau, France.

[4]Aix-Marseille Université, CEA, CNRS, BIAM, 13108 Saint Paul lez Durance, France.

Abstract

Crystallization from solution is commonly described by classical nucleation theory, although this ignores that crystals often form via disordered nanostructures. As an alternative, the classical theory remains widely used in a "multi-step" variant, where the intermediate nanostructures merely introduce additional thermodynamic parameters. But this variant still requires validation by experiments addressing indeed proper time and spatial scales (ms, nm). Here, we used *in situ* X-ray scattering to determine the mechanism of magnetite crystallization and in particular how nucleation propagates at the nanometer scale within amorphous precursors. We find that the self-confinement by an amorphous precursor slows down crystal growth by two orders of magnitude once the crystal size reaches the amorphous particle size (c.a. 3 nm). Thus, not only the thermodynamic properties of transient amorphous nanostructures, but also their spatial distribution determine crystal nucleation.

KEYWORDS: magnetite, nanoparticles, nucleation, *in situ* SAXS/WAXS, classical nucleation theory, non-classical crystallization

TOC IMAGE

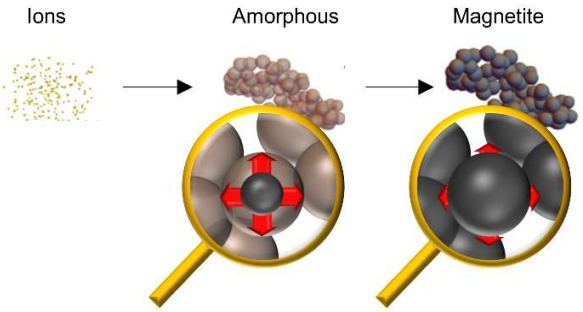

Text

Crystallization of solids from dilute solutions governs the formation of many synthetic, biogenic and geologic minerals.[1] This ubiquitous process has long been described by "classical" nucleation theory (CNT): crystal nuclei capture or release solute monomers through thermal fluctuations; nuclei that reach the critical size, where the energetic gain of the new phase compensates the cost of the crystal/solvent boundary, finally grow faster than they dissolve and reach macroscopic sizes. This model allows calculating nucleation rates, *i.e.* the number of new crystals formed per unit time:[2,3]

$$J^{\mathrm{st}} = Ae^{\frac{-W(N^*)}{kT}} \qquad (1)$$

This expression combines i) the thermodynamic parameters of the crystal, which through the Boltzmann factor $e^{\frac{-W(N^*)}{kT}}$ express the probability to successfully cross the activation barrier $W(N^*)$, i.e. the minimal work of formation of a cluster of critical size N^* and ii) a kinetic prefactor $A = \bar{n}_1 Z(N^*)k^+(N^*)$, where $Z(N^*)$ is the Zeldovich factor that corrects for the width of the activation barrier (see SI), $\bar{n}_1$ is the concentration of monomers in the metastable phase, and $k^+(N^*)$ is the rate of monomer addition to a cluster of size N^*. k^+ relates to the rate of growth and the rate of monomer loss by a cluster of size N+1 *via* $k(N) = k^+(N) - k^-(N+1)$.

However, the relevance of this theory is questioned since recent experimental evidence has pointed towards crystals forming through complex reactions with possible amorphous intermediate states,[1,4–13] in contradiction with the founding hypotheses of the CNT that overlooks any intermediate amorphous cluster by design. In the course of the reaction, solutes may enrich in droplets, form polymers, clusters and nanoparticles that only crystallize later, leading to a so-called "non-classical" nucleation scenario. As a consequence, not only the hypotheses of the theory are

incompatible with experiments, but also the predictions of the nucleation rates are inconsistent by several tens of orders of magnitude.[5,6]

To reach a better theoretical description of crystallization, a common approach is to apply the classical nucleation theory to intermediate steps, *i.e.* the nucleation of an intermediate phase from a metastable solution, followed by the nucleation of the crystals from the intermediate phase.[5,14] This approach leads to the definition of the consecutive activation barriers from corrected thermodynamic parameters: the free energy of reaction g then accounts for the reaction to or from the intermediate phase, and the interfacial free energy γ accounts for interface creation between the intermediate phase and the initial and the final states, respectively.[5,6,10,14] These corrections to the classical nucleation theory allow fitting the predicted nucleation rates to the measurements and extracting effective thermodynamic parameters. In other words, the classical nucleation theory has been made compatible with the "non classical" cases, although the retrieved thermodynamic parameters to describe those phase transitions at the nanometer scale far from equilibrium have remained controversial, affecting their predictive usefulness.

By contrast, there has been little consideration of the kinetic prefactor A, although it allows in principle a strong consistency test of the classical nucleation theory. On the one hand, A can be measured easily from the variation of nucleation rates with reactant concentration similarly to the thermodynamic parameters. On the other hand, the classical nucleation theory imposes two conditions: i) the kinetic prefactor must relate to the forward rate of monomer addition $k^+(N^*)$ at the critical size via $A = \bar{n}_1 Z(N^*)k^+(N^*)$, and ii) the forward rate of monomer addition $k^+(N)$ must relate to the net growth rate $k=k^+ - k^-$ due to the constrained equilibrium hypothesis used to derive the nucleation rates in the CNT:[2]

$$k(N) = k^+(N) - k^+(N-1)e^{\frac{W(N)-W(N-1)}{kT}} \qquad (2)$$

Therefore, not only the nucleation rate, but also the growth rate must remain consistent with the thermodynamic constants of the transition and the transport properties from the metastable phase to the stable phase. However, the coupled analysis of the nucleation rates and growth rates requires time-resolved, structural data at crystal sizes of only a few structural units, which are out of reach of the techniques commonly used in the seminal studies on non-classical nucleation: potentiometry, cryo-TEM, optical microscopy, or atomic force microscopy to name a few.[5,10–13,15–17] They provide necessary qualitative information on the formation of the nanoparticles and their aggregation (e.g. the "crystallization per attachment" process),[17] but lack a quantitative assessment of the nucleation of the primary crystals themselves as may be provided by small and wide angle X-ray scattering (SAXS).[8,18]

Here we resolve at appropriate nanoscale and millisecond resolutions the crystallization of magnetite (Fe_3O_4) nanoparticles, a paradigmatic example of a synthetic, biogenic and geologic iron oxide known to crystallize from disordered precursors.[10,19–22] Dispersions of magnetite nanoparticles in water with a total iron concentration c = 5mM, 12.5mM, 25mM, 37.5mM and 50mM range were synthesized by mixing two equal volumes of a) an aqueous solution of $FeCl_2$ and $FeCl_3$ with respective concentrations c/3 and 2c/3, acidified with 0.1M HCl, and b) a 1M NaOH solution (see Materials and Methods in SI). The mixing was carried out in fast millifluidic and stopped-flow mixers and characterized by synchrotron *in situ* X-ray small- and wide-angle scattering (SAXS/WAXS) on the SOLEIL/Swing beamline.[23] It enabled us to resolve the developing nanostructures over several length (0.1 – 100 nm) and time scales (0.4 - 600 s) (Fig. 1 for c = 37.5mM).

At the shortest observed reaction time (400 ms) up to 15 s of reaction, we evidence that most of the reactants are involved into fractal aggregates of sub-nanometer, amorphous iron

(oxyhydr)oxide particles. The lack of long-range crystalline order is evidenced by the absence of detectable Bragg peaks in the WAXS signal, while the total scattered signal in the SAXS range is orders of magnitude beyond the detection limit. The fractal aggregation is characterized by a scattering signal decaying as a power low at low angles, before reaching a shoulder at $q \approx 0.2$-0.5 Å^{-1}. The aggregates consisted of particles with a radius of gyration of $R_g = 0.5 \pm 0.1$ nm after 150 ms and grew to $R_g = 1.2 \pm 0.1$ nm within 15 s as determined from SAXS modeling (Supplementary Figure 3). This corresponds to spherical particles of 1.3 nm growing to 3 nm in diameter.

Afterwards, these amorphous particles crystallized to magnetite as evident from appearing Bragg reflections in WAXS (Fig. 1b). The total volume of amorphous and crystal phases is evaluated from the total scattering intensity ("invariant theorem", see Materials and Methods in SI):[24]

$$Q = 4\pi \int_0^{+\infty} I(q) q^2 dq = (2\pi)^3 < \eta^2 > \qquad (3)$$

where $< \eta^2 >$ is the quadratic mean fluctuation of scattering length density. Observing that Q remains constant during the amorphous-to-crystal conversion, we assume that the electron density of the amorphous and crystal are identical within the experimental resolution, and find that the amorphous-to-crystal conversion occurs at constant volume fraction ϕ_{tot} (Fig. 2a), given by:[24]

$$< \eta^2 >= \phi_{tot}(1 - \phi_{tot})\Delta\rho^2 \qquad (4)$$

with $\Delta\rho = \rho - \rho_{H_2O}$ the constrast of scattering length density with water.

The hypothesis on the electron densities of the amorphous and crystal being equal has been validated *a posteriori* by i) the consistency between the total volume fractions evaluated by the integration of the SAXS, and expected from the total iron concentration (Fig. 2a black circles and blue dashed line), and ii) the consistency between the crystal volume fraction evaluated by the

integration of the WAXS, and by the integration of the contribution of the crystals to the SAXS (see below and Fig. 2a red symbols).

We extracted selectively the structural parameters of the crystals, *i.e.* the volume fractions (Fig. 2a), sizes (Fig. 2b and 2c) and concentrations (Fig. 2d). The treatment (see all details in SI) consists in i) after calculating the advancement of reaction as evaluated by integration of the Bragg peaks, subtracting the proper proportion of the signal of the initial amorphous network, and ii) fitting to the thus extracted contribution of the crystals, a model describing mass fractal aggregates of nanocrystals. We find that the crystal volume fractions evaluated by the integration of the WAXS, and by the integration of the crystal SAXS signal are identical within experimental accuracy (Fig. 2a red symbols), supporting in particular i) the good sensitivity of the WAXS detection, ii) that the electron densities of the amorphous and crystal phase are identical within experimental resolution, and iii) that any evolution of the amorphous phase during crystallization do not significantly affect our treatment.

The structural parameters of the crystals enabled us to identify a nucleation/growth stage followed by an aggregation stage. Both stages were observable at Fe concentrations of 37.5 and 50 mM, where: (i) during the nucleation/growth period, concentrations and sizes of crystals grew continuously, and (ii) during aggregation, crystal concentrations decreased while particles diameters grew from 4±0.2 nm to 8±0.3 nm. Simultaneously, the total crystal volume fraction still increased, evidencing that this "crystallization par aggregation" stage[17] is accompanied by a residual growth stage. At lower Fe concentration (17.5 mM and 25mM), no aggregation was observed, and at Fe concentrations of 5 mM, the precursors did not crystallize within the investigated time frame also upon drying as observed by TEM (Supplementary Figure 3). At the

largest concentration (50 mM), the nucleation is ill-resolved because of the overlap with aggregation, and the nucleation rate was excluded from the analysis.

From the evolution of the volume fraction and of number of crystals, we evaluated both the crystal nucleation rate J^{st} and the net growth rate k of the crystals by addition of iron units from the amorphous precursor. The number of crystals produced per unit time and solution volume during the steady-state regime $J^{st} = \partial\bar{n}/\partial t$, as estimated from the linear increase in crystal concentrations during the nucleation periods (Fig. 2d, dashed lines), increases from (1.1±0.2) 10^{20} $m^{-3}s^{-1}$ to (6.7±1.4) 10^{20} $m^{-3}s^{-1}$ with concentration (Fig. 3a, circles). The lowest measurable size N_0 is between 230±140 and 470±80 structural units (Fig. 2c), reached within Δt < 1s of reaction. At these sizes, the crystals grow at a rate k between 4.2±0.3 to 9.6±2.3 structural units per second (Fig. 3b, circles), as evaluated from the increase in volume of the crystals (Fig. 2c).

We evidence the collapse in the growth rate by a lack of consistency between J^{st}, N_0 and k, in two possible scenarios: dissolution-recrystallization and crystallization within the dense phase. In a dissolution-recrystallization mechanism, the amorphous particles are in equilibrium with ions in solution and impose a solute concentration of ions s_{amorph}. This solubility of the amorphous phase must be significantly smaller than c.a. 5% the nominal iron concentration (c), given that all iron species are in the solid phases within the SAXS resolution (Fig. 2a, black lines and circles). Yet, s_{amorph} could be higher than the solubility of the crystal s_{cryst}.[25] Crystallization then occurs by addition of dissolved iron species:

$$\text{(Amorphous)} \leftrightharpoons 2\ Fe(OH)_a^{3-a} + Fe(OH)_b \rightarrow Fe_3O_4 + (2a+b-8)\ OH^- + 4\ H_2O$$

where (a, b) account for the speciation of iron in the high-pH medium. To compare the experimental and theoretical data, we have measured the standard free energy of crystallization (g^0 = -17.9 kT per structural unit, or -131 kJ per mole of Fe_3O_4, i.e. a bulk crystal solubility of

s_{cryst}=3·10^{-2} µmol.L^{-1}), and the interfacial tension of the crystal/water boundary (σ= 0.16 J.m^{-2}) by measuring the solubility of the magnetite nanocrystals as a function of size (SI).

Estimating that the amorphous solubility cannot exceed s_a = 1 mmol.L^{-1}, an upper limit for the activation barrier can be evaluated as $W(N^*) \leq 15kT$ by using $e^{-\frac{W(N^*)}{kT}} \simeq \frac{J^{st}}{[Z(N^*)k^+(N^*)\bar{n}_1]}$ with $J^{st} \simeq 10^{20}$m^{-3}s^{-1}, $Z(N^*) \simeq 1$, and a forward rate of attachment $k^+(N^*) \leq 10^8$s^{-1} that cannot exceed the feed rate by diffusion (SI). On the other hand, $W(N^*) = \frac{1}{2}N^*|g|$ with the free energy of reaction per structural unit $g = kT \log \frac{s_{cryst}}{s_{amorph}}$ of the order of -10 kT. Therefore, the critical size N^* cannot exceed a few structural units. As a consequence, the mean rate of growth k_0 between the critical size N^* and the minimal observable size N_0, given by:

$$N_0 = N^* + k_0\Delta t \qquad (5)$$

is in the order of k_0 = 100 to 500 s^{-1}. In other words, the mean rate of growth below N_0 is significantly larger than the rate of growth k = 4 to 10 s^{-1} observed above N_0.

A more quantitative evaluation of the kinetics expected for dissolution / reprecipitation shows that the slowdown of growth is even stronger. We used Eq. 1, 2 and 3 with the amorphous solubility s_{amorph} as the single free parameter to fit the predicted and the experimental nucleation rates, assuming that crystallization is either diffusion-limited (DL, $k^+(r) \propto r$ as given by the Smoluchowski equation, SI), or rate-limited (RL, $k^+(r) \propto r^2$). In any case, the best agreements between experimental and theoretical nucleation rates are found for amorphous solubilities that are in a reasonable range (6 µmol.L^{-1} for DL, 16 µmol.L^{-1} for RL). But we find that the growth rate from the critical size (5 to 10 structural units) up to N_0 is indeed several orders of magnitude faster than just above N_0 (k_0 = 510±25 s^{-1} for RL to (1.6±0.1) 10^5 s^{-1} for DL against k = 4 to 10 s^{-1}, Fig. 3). A collapse of the growth rate needs be invoked to support the scenario of dissolution-

recrystallization, but it is not physically consistent with reactant depletion in the liquid phase. Indeed, diffusion in water feeds the crystals at a typical rate of 10^8 s^{-1} (SI), largely sufficient to compensate for the consumption by the reaction (c.a. 510 to 10^5 s^{-1}). Therefore, we rule out the dissolution-recrystallization mechanism because of the collapse of the growth rate at N_0.

Alternatively, crystallization can occur by direct transformation of the amorphous particles, assuming that they have a net structural charge of $-\nu$ per iron atom:

$$(\text{Amorphous})^{-\nu} \rightarrow \text{Fe}_3\text{O}_4 + \nu\,\text{OH}^- + h\,\text{H}_2\text{O}$$

Crystal nucleation within an amorphous precursor belongs to the scope of the classical nucleation theory: as assumed by the CNT, a single order parameter fluctuates (size of the nascent phase), not two (the size and the density). Instead of the prediction for the nucleation rate expressed per unit of solution volume (eq. 1), we use the nucleation rate per unit volume of dense metastable phase:

$$J^{\text{dense}} = J^{\text{solution}}/\phi_{\text{amorphous}} = k^+(N^*)Z(N^*)\bar{n}_1^{\text{dense}} e^{\frac{-W(N^*)}{kT}} \qquad (6)$$

where $\phi_{\text{amorphous}}$ is the volume fraction of dense phase, and $\bar{n}_1^{\text{dense}}$ is the density of the amorphous phase (number of structural units per volume unit). As practically all reactants are present in the amorphous particles, the nucleation rate expressed per unit volume of solution takes the same expression as eq. 1, where the nominal concentration of iron species $\bar{n}_1^{\text{nominal}}$ is used instead of the solubility of the amorphous particles $\bar{n}_1^{\text{solution}}$. Furthermore, we consider that the crystallization is rate-limited instead of diffusion-limited, owing to the short interatomic distances in the amorphous particles. The free energy of reaction from the amorphous particles to the crystal is unknown, but we observe that at thermodynamic equilibrium, the fraction of iron in the crystal dominates the fraction of iron under the form of amorphous particles by at least factor of 10^2 (Fig. 2a). Therefore, the free energy of formation of the crystal from the amorphous particles is at least

$|g| \geq kT \ln 10^2 \simeq 5\, kT$. Following the same qualitative argument as above, the critical size N^* must be significantly lower than N_0 to avoid unphysical activation barriers of 500 kT.

More quantitatively for a given value of g, the only free parameter in eq. 1 to 3 to fit the predicted nucleation rates to the data is then the interfacial tension between amorphous particles and magnetite crystals (Fig. 4). Independently on the assumed value of g, we find that the critical size is at most 10 Fe structural units, and the growth rate from N^* to N_0 is 500 s^{-1}, again up to *c.a.* 2 orders of magnitude faster than measured at N_0 (4 to 10 s^{-1}). Therefore, we unveil a collapse of the growth rate when the size of the crystals reaches c.a. 3 nanometer in diameter, identical to the diameter of the amorphous particles. In case of dissolution-recrystallization, the slowdown of the growth would have no clear physical origin; by contrast, it is consistent with the direct amorphous-to-crystal transition, and is assigned to reaction confinement in the solid-state amorphous matrix. As a matter of fact, the inconsistency between J^{st}, N_0 and k is so strong it can be unveiled on qualitative grounds only as shown above, regardless of the details of the chemical reactions and structural rearrangements known to occur,[16] and excludes any crystallization scenario unless a confinement by the reactants is invoked.

As a result, the values of k_0 indicate that within a second, several hundreds of structural units are transferred from the amorphous particles to the nascent crystal. The growth rate then abruptly decays because the crystals have depleted the amorphous particles, and grow by transfer from the ions in solution. We expect that such a self-confinement effect is dominant when the characteristic time τ to reach a critical fluctuation to form a crystal in the amorphous volume of characteristic size ξ, which scales as $\tau \propto \frac{1}{J^{\mathrm{dense}} \xi^3} \simeq 1\mu s$, is shorter than the lifetime of the amorphous particle. Therefore, the precursor nanostructure is irrelevant for a proper description of nucleation from large droplets of liquid precursors as for example in $CaCO_3$.[26] In contrast, in any sufficiently small,

viscous and/or insoluble nucleation precursor (small liquid droplets, amorphous nanoparticles, solid-state or gel-like aggregates), not only the thermodynamic properties of the amorphous precursor, but also the characteristic length ξ has to be accounted for, in order to accurately predict the crystallization mechanism, hence the number of crystals and their final sizes. In particular, the dissolution / recrystallization scenario must be absent, or at least sufficiently slow, as we have evidenced here by analysis of the kinetic constants.

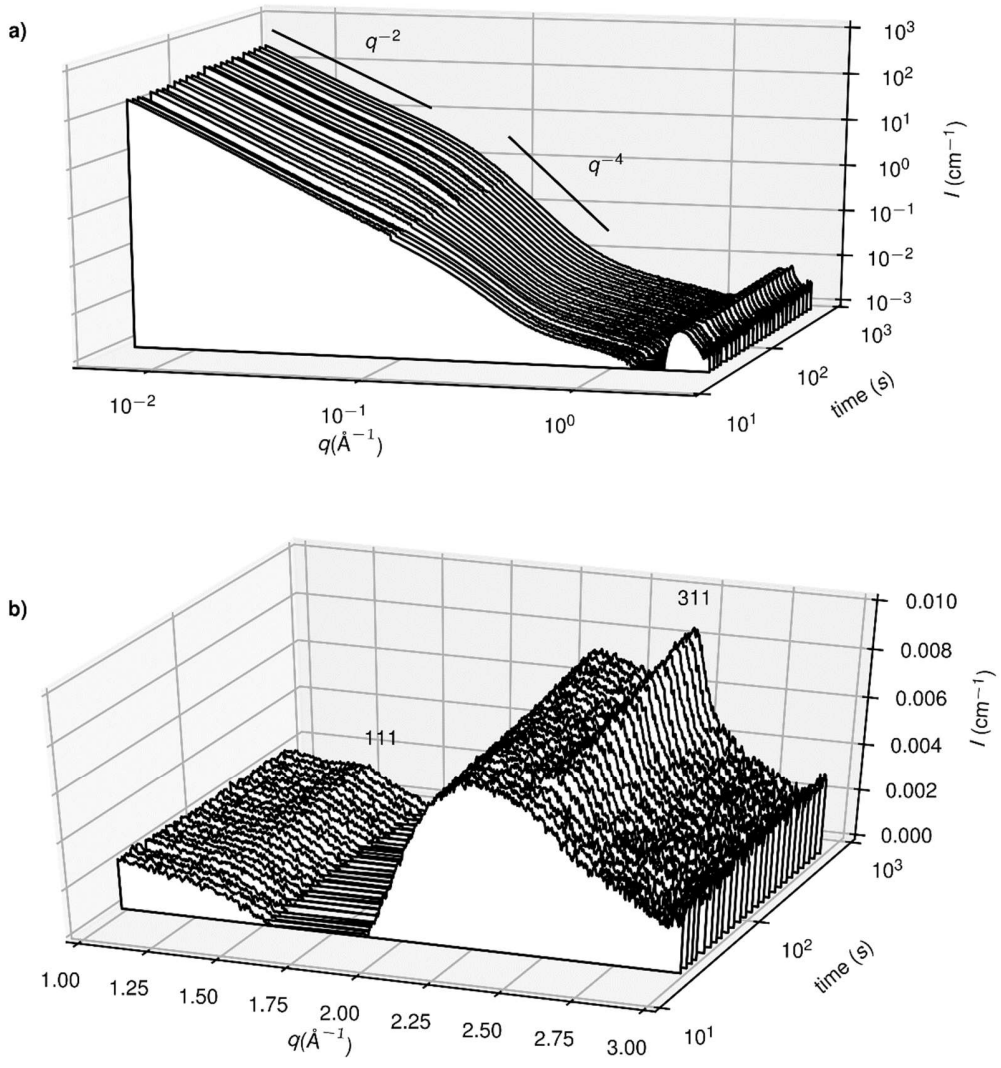

Figure 1. Time evolution of the X-ray scattering patterns during magnetite synthesis with a total iron concentration of 37.5 mM. From the SAXS patterns (**a**), we infer that nanostructured, extended aggregates are formed from the lowest measured reaction time. The WAXS patterns (**b**) indicate that the aggregates are first amorphous and then crystallize into magnetite.

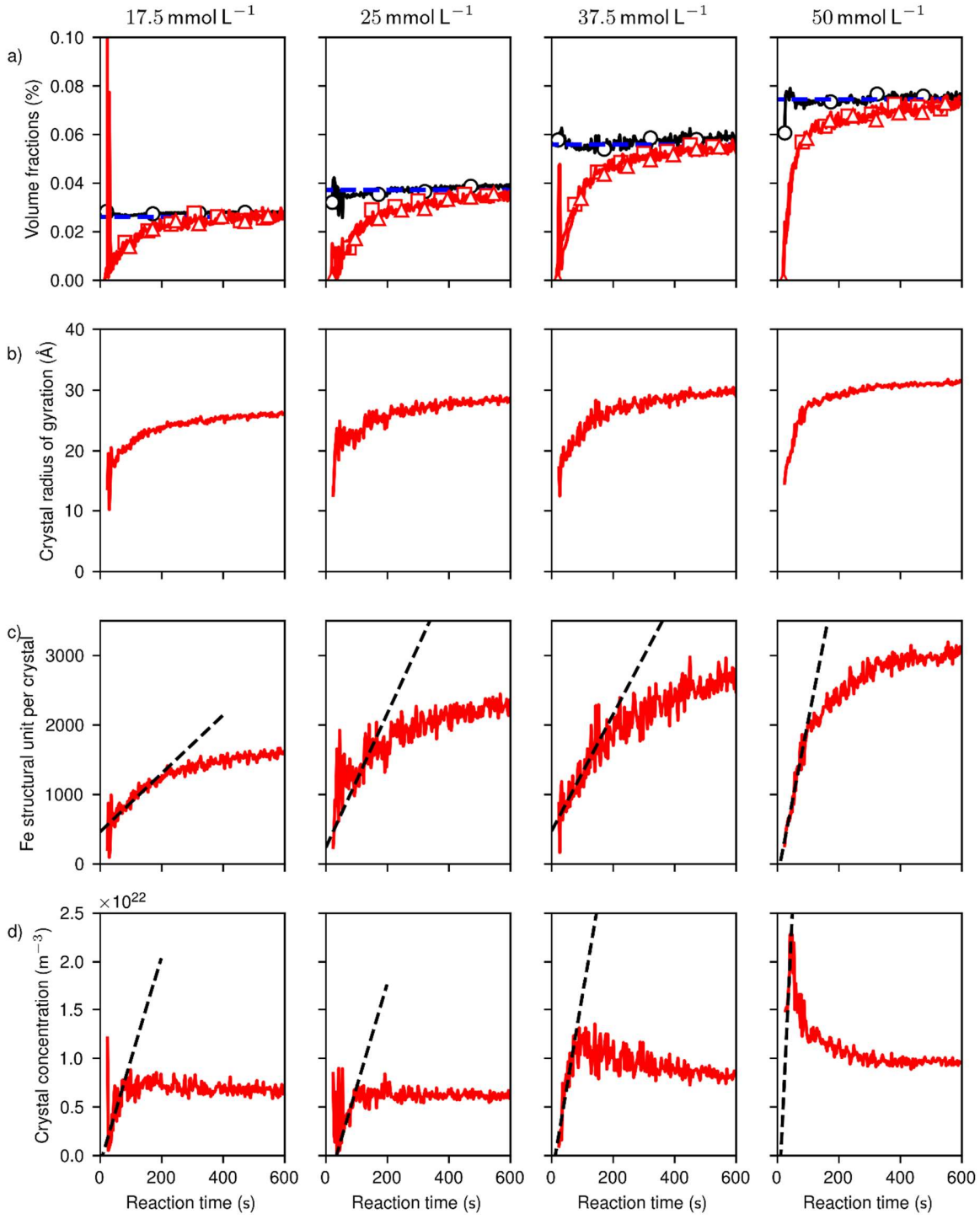

Figure 2. Physical parameters extracted from the scattering patterns at different iron concentrations. (**a**) Total volume fraction of condensed phase (circles), volume fraction of crystalline phase from Bragg peak integration (triangles) and SAXS analysis (squares). The blue

line indicates the maximal crystalline volume fractions expected from c_{Fe}. (**b**) Radius of gyration of the crystalline particles. (**c**) Number of $FeO_{4/3}$ structural unit per crystal. (**d**) Numeric concentration of crystalline particles. The dashed lines are linear regressions used to retrieve the growth rate and nucleation rate.

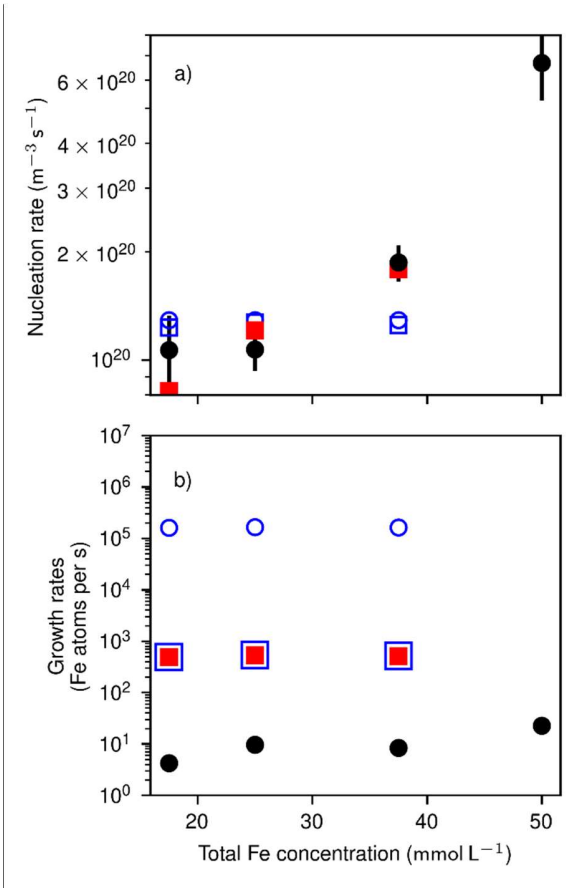

Figure 3. Comparison of experimental and theoretical (**a**) nucleation rates, and (**b**) growth rates. Full black circles: experimental data. Full red squares: assuming a rate-limited growth within the amorphous particles. Blue squares: assuming a rate-limited dissolution-recrystallization. Blue circles: assuming a diffusion-limited dissolution-recrystallization.

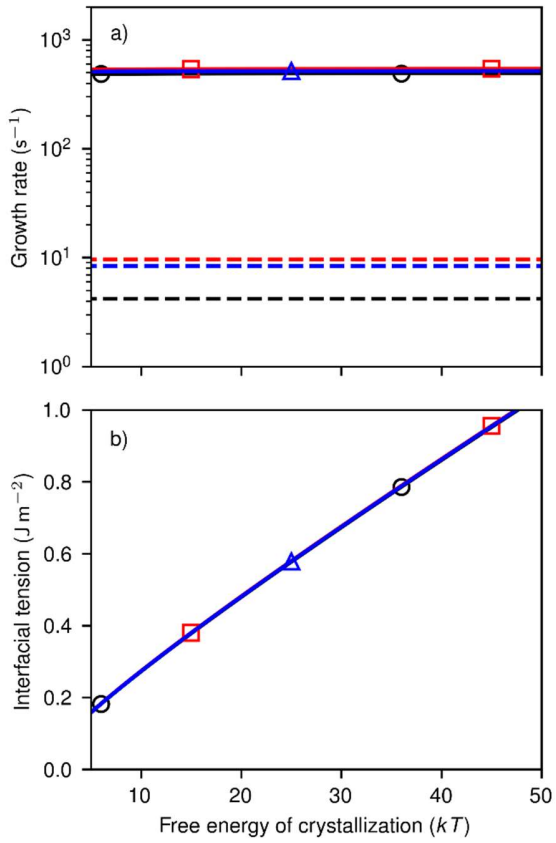

Figure 4. Kinetic and thermodynamic parameters determined after fitting the theoretical to the experimental nucleation rates and the crystal sizes. a) Mean growth rate between the critical size and the minimal observable size as a function of the assumed free energy of crystallization from the amorphous precursor, and b) interfacial energy. Black circles: using [Fe] = 17.5 mM, red squares: [Fe] = 25 mM, blue triangles: [Fe] = 37.5 mM. The dashed lines indicate the experimental growth rates.

Supporting Information.

The following files are available free of charge: Materials and methods, X-ray powder diffraction, Size-dependent solubility of formed magnetite nanoparticles, SAXS data from a stopped-flow configuration, Deconvolution of the crystals contribution to the SAXS signal, Transmission electron microscopy images and Additional references (PDF).

Corresponding Author

*Correspondance should be addressed to david.carriere@cea.fr or damien.faivre@cea.fr

Present Addresses

†Laboratoire de Génie Chimique, Université de Toulouse, CNRS, INPT, UPS, Toulouse, France.

Author Contributions

‡These authors contributed equally.

ACKNOWLEDGMENT

The authors acknowledge the SOLEIL synchrotron for beamtime. We thank Jeannette Steffen (MPI) for ICP-OES, and Corinne Chevallard, Thierry Gacoin, Jean-Baptiste Champenois, Mathias Egglseder and Yael Politi for discussions. APF, MAN, and DC acknowledge a public grant overseen by the French National Research Agency (ANR), project DIAMONS ANR-14-CE08-0003. RKR acknowledges support by ANR as part of the "Investissements d'Avenir" program (Labex NanoSaclay, reference: ANR-10-LABX-0035). DF was supported by the Max Planck Society, the DFG (DFG-ANR project (FA 835/10-1)), and the European Research Council through a Starting Grant 256915-MB2.

REFERENCES

(1) Yoreo, J. J. D.; Gilbert, P. U. P. A.; Sommerdijk, N. A. J. M.; Penn, R. L.; Whitelam, S.; Joester, D.; Zhang, H.; Rimer, J. D.; Navrotsky, A.; Banfield, J. F.; Wallace, A. F.; Michel, F. M.; Meldrum, F. C.; Cölfen, H.; Dove, P. M. Crystallization by Particle Attachment in Synthetic, Biogenic, and Geologic Environments. *Science* **2015**, *349* (6247), aaa6760. https://doi.org/10.1126/science.aaa6760.

(2) Kelton, K.; Greer, A. L. *Nucleation in Condensed Matter: Applications in Materials and Biology*; Pergamon materials series; Elsevier: Amsterdam, 2010.

(3) Becker, R.; Döring, W. Kinetische Behandlung Der Keimbildung in Übersättigten Dämpfen. *Ann. Phys.* **1935**, *416* (8), 719–752. https://doi.org/10.1002/andp.19354160806.

(4) Lee, J.; Yang, J.; Kwon, S. G.; Hyeon, T. Nonclassical Nucleation and Growth of Inorganic Nanoparticles. *Nat. Rev. Mater.* **2016**, *1* (8), natrevmats201634. https://doi.org/10.1038/natrevmats.2016.34.

(5) Habraken, W. J. E. M.; Tao, J.; Brylka, L. J.; Friedrich, H.; Bertinetti, L.; Schenk, A. S.; Verch, A.; Dmitrovic, V.; Bomans, P. H. H.; Frederik, P. M.; Laven, J.; van der Schoot, P.; Aichmayer, B.; de With, G.; DeYoreo, J. J.; Sommerdijk, N. A. J. M. Ion-Association Complexes Unite Classical and Non-Classical Theories for the Biomimetic Nucleation of Calcium Phosphate. *Nat. Commun.* **2013**, *4*, 1507. https://doi.org/10.1038/ncomms2490.

(6) Vekilov, P. G. Nucleation. *Cryst. Growth Des.* **2010**, *10* (12), 5007–5019. https://doi.org/10.1021/cg1011633.

(7) Smeets, P. J. M.; Finney, A. R.; Habraken, W. J. E. M.; Nudelman, F.; Friedrich, H.; Laven, J.; Yoreo, J. J. D.; Rodger, P. M.; Sommerdijk, N. A. J. M. A Classical View on Nonclassical Nucleation. *Proc. Natl. Acad. Sci.* **2017**, 201700342. https://doi.org/10.1073/pnas.1700342114.

(8) Fleury, B.; Neouze, M.-A.; Guigner, J.-M.; Menguy, N.; Spalla, O.; Gacoin, T.; Carriere, D. Amorphous to Crystal Conversion as a Mechanism Governing the Structure of Luminescent YVO4:Eu Nanoparticles. *ACS Nano* **2014**, *8* (3), 2602–2608. https://doi.org/10.1021/nn4062534.

(9) Legg, B. A.; Zhu, M.; Zhang, H.; Waychunas, G.; Gilbert, B.; Banfield, J. F. A Model for Nucleation When Nuclei Are Nonstoichiometric: Understanding the Precipitation of Iron Oxyhydroxide Nanoparticles. *Cryst. Growth Des.* **2016**, *16* (10), 5726–5737. https://doi.org/10.1021/acs.cgd.6b00809.

(10) Baumgartner, J.; Dey, A.; Bomans, P. H. H.; Le Coadou, C.; Fratzl, P.; Sommerdijk, N. A. J. M.; Faivre, D. Nucleation and Growth of Magnetite from Solution. *Nat. Mater.* **2013**, *12* (4), 310–314. https://doi.org/10.1038/nmat3558.

(11) Gebauer, D.; Völkel, A.; Cölfen, H. Stable Prenucleation Calcium Carbonate Clusters. *Science* **2008**, *322* (5909), 1819–1822. https://doi.org/10.1126/science.1164271.

(12) Pouget, E. M.; Bomans, P. H. H.; Goos, J. A. C. M.; Frederik, P. M.; With, G. de; Sommerdijk, N. A. J. M. The Initial Stages of Template-Controlled CaCO3 Formation Revealed by Cryo-TEM. *Science* **2009**, *323* (5920), 1455–1458. https://doi.org/10.1126/science.1169434.

(13) Dey, A.; Bomans, P. H. H.; Müller, F. A.; Will, J.; Frederik, P. M.; With, G. de; Sommerdijk, N. A. J. M. The Role of Prenucleation Clusters in Surface-Induced Calcium Phosphate Crystallization. *Nat. Mater.* **2010**, *9* (12), 1010–1014. https://doi.org/10.1038/nmat2900.

(14) Kashchiev, D.; Vekilov, P. G.; Kolomeisky, A. B. Kinetics of Two-Step Nucleation of Crystals. *J. Chem. Phys.* **2005**, *122* (24), 244706. https://doi.org/10.1063/1.1943389.
(15) Galkin, O.; Vekilov, P. G. Control of Protein Crystal Nucleation around the Metastable Liquid–Liquid Phase Boundary. *Proc. Natl. Acad. Sci.* **2000**, *97* (12), 6277–6281. https://doi.org/10.1073/pnas.110000497.
(16) Jensen, K. M. Ø.; Andersen, H. L.; Tyrsted, C.; Bøjesen, E. D.; Dippel, A.-C.; Lock, N.; Billinge, S. J. L.; Iversen, B. B.; Christensen, M. Mechanisms for Iron Oxide Formation under Hydrothermal Conditions: An in Situ Total Scattering Study. *ACS Nano* **2014**, *8* (10), 10704–10714. https://doi.org/10.1021/nn5044096.
(17) Mirabello, G.; Ianiro, A.; Bomans, P. H. H.; Yoda, T.; Arakaki, A.; Friedrich, H.; With, G. de; Sommerdijk, N. A. J. M. Crystallization by Particle Attachment Is a Colloidal Assembly Process. *Nat. Mater.* **2019**, 1–6. https://doi.org/10.1038/s41563-019-0511-4.
(18) Stawski, T. M.; Driessche, A. E. S. van; Ossorio, M.; Rodriguez-Blanco, J. D.; Besselink, R.; Benning, L. G. Formation of Calcium Sulfate through the Aggregation of Sub-3 Nanometre Primary Species. *Nat. Commun.* **2016**, *7*, ncomms11177. https://doi.org/10.1038/ncomms11177.
(19) Cornell, R. M.; Schwertmann, U. *The Iron Oxides: Structure, Properties, Reactions, Occurrences and Uses*; Wiley-VCH: Weinheim, 2003.
(20) Faivre, D.; Schüler, D. Magnetotactic Bacteria and Magnetosomes. *Chem. Rev.* **2008**, *108* (11), 4875–4898. https://doi.org/10.1021/cr078258w.
(21) Laurent, S.; Forge, D.; Port, M.; Roch, A.; Robic, C.; Vander Elst, L.; Muller, R. N. Magnetic Iron Oxide Nanoparticles: Synthesis, Stabilization, Vectorization, Physicochemical Characterizations, and Biological Applications. *Chem. Rev.* **2008**, *108* (6), 2064–2110. https://doi.org/10.1021/cr068445e.
(22) Sun, S.; Gebauer, D.; Cölfen, H. Alignment of Amorphous Iron Oxide Clusters: A Non-Classical Mechanism for Magnetite Formation. *Angew. Chem. Int. Ed.* **2017**, *56* (14), 4042–4046. https://doi.org/10.1002/anie.201610275.
(23) David, G.; Pérez, J. Combined Sampler Robot and High-Performance Liquid Chromatography: A Fully Automated System for Biological Small-Angle X-Ray Scattering Experiments at the Synchrotron SOLEIL SWING Beamline. *J. Appl. Crystallogr.* **2009**, *42* (5), 892–900. https://doi.org/10.1107/S0021889809029288.
(24) *Neutrons, X-Rays and Light: Scattering Methods Applied to Soft Condensed Matter*, 1. ed.; Lindner, P., Zemb, T., Eds.; North-Holland delta series; Norh-Holland, Elsevier: Amsterdam, 2002.
(25) Putnis, A. Why Mineral Interfaces Matter. *Science* **2014**, *343* (6178), 1441–1442. https://doi.org/10.1126/science.1250884.
(26) Wallace, A. F.; Hedges, L. O.; Fernandez-Martinez, A.; Raiteri, P.; Gale, J. D.; Waychunas, G. A.; Whitelam, S.; Banfield, J. F.; De Yoreo, J. J. Microscopic Evidence for Liquid-Liquid Separation in Supersaturated CaCO3 Solutions. *Science* **2013**, *341* (6148), 885–889. https://doi.org/10.1126/science.1230915.